ACSNANO
www.acsnano.org
ARTICLE

Production of Highly Monolayer Enriched Dispersions of Liquid-Exfoliated Nanosheets by Liquid Cascade Centrifugation

Claudia Backes,[†,‡] Beata M. Szydłowska,[†,‡] Andrew Harvey,[†,‡] Shengjun Yuan,[§] Victor Vega-Mayoral,[∥,⊥] Ben R. Davies,[†,‡] Pei-liang Zhao,[#] Damien Hanlon,[†,‡] Elton J. G. Santos,[▽] Mikhail I. Katsnelson,[§] Werner J. Blau,[†,‡] Christoph Gadermaier,[∥,⊥] and Jonathan N. Coleman*[,†,‡]

[†]CRANN & AMBER Research Centers, Trinity College Dublin, Dublin 2, Ireland

[‡]School of Physics, Trinity College Dublin, Dublin 2, Ireland

[§]Institute for Molecules and Materials, Radboud University of Nijmegen, Heijendaalseweg 135, 6525AJ Nijmegen, The Netherlands

[∥]Department for Complex Matter, Jozef Stefan Institute, Jamova 39, 1000 Ljubljana, Slovenia

[⊥]Jozef Stefan International Postgraduate School, Jamova 39, 1000 Ljubljana, Slovenia

[#]Department of Applied Physics, Zernike Institute for Advanced Materials, University of Groningen, Nijenborgh 4, NL-9747AG Groningen, The Netherlands

[▽]School of Mathematics and Physics and School of Chemistry and Chemical Engineering, Queen's University Belfast, Belfast, BT95AL, United Kingdom

Supporting Information

ABSTRACT: **While liquid exfoliation is a powerful technique to produce defect-free nanosheets in large quantities, its usefulness is limited by broad nanosheet thickness distributions and low monolayer contents. Here we demonstrate liquid processing techniques, based on iterative centrifugation cascades, which can be designed to achieve either highly efficient nanosheet size-selection and/or monolayer enrichment. The resultant size-selected dispersions were used to establish quantitative metrics to determine monolayer volume fraction, as well as mean nanosheet size and thickness, from standard spectroscopic measurements. Such metrics allowed us to design and optimize centrifugation cascades to enrich liquid exfoliated WS_2 dispersions up to monolayer contents of 75%. Monolayer-rich dispersions show relatively bright photoluminescence with narrow line widths (<35 meV) indicating the high quality of the nanosheets. The enriched dispersions display extinction spectra with distinct features, which also allow the direct estimation of monolayer contents.**

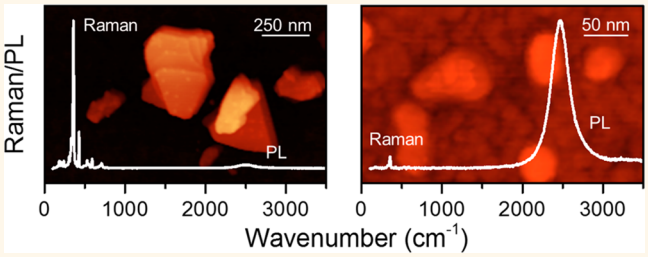

KEYWORDS: *exfoliation, monolayer, size-selection, luminescence, tungsten disulfide*

Liquid phase exfoliation is a versatile technique for producing liquid suspensions containing large quantities of 2-dimensional (2D) nanosheets.[1−7] This method involves the sonication[2,4] or shearing[8,9] of layered materials in liquids, resulting in the production of generally defect-free nanosheets. If the liquid is appropriately chosen (*e.g.*, suitable solvents[5,6,10,11] or surfactant[3,12−15] or polymeric solutions[16−19]) the nanosheets will be stabilized against reaggregation.[20] This method has been used to exfoliate a broad range of 2D materials including graphene,[2,6,9,12,17,21] BN,[5] transition metal dichalcogenides such as MoS_2 and WSe_2,[4,8,22,23] as well as MoO_3,[24,25] GaS,[26] black phosphorus[27−31] and MXenes.[32] The liquid suspensions produced in this way are extremely useful, as they can be easily processed into a range of structures including films, coatings and composites.[5,23,33−35] Such materials have demonstrated superlative performance in a number of applications including reinforced composites,[5,18,36,37] battery electrodes[38,39] and fiber lasers.[40−42]

However, liquid phase exfoliation tends to give nanosheets with very broad lateral size (length, L) and thickness (expressed as number of monolayers per nanosheet, N) distributions,[15,43] with ranges of 50 nm ≤ L ≤ 500 nm and 1 ≤ N ≤ 10 not

Received: November 16, 2015
Accepted: January 5, 2016

DOI: 10.1021/acsnano.5b07228
ACS Nano XXXX, XXX, XXX−XXX

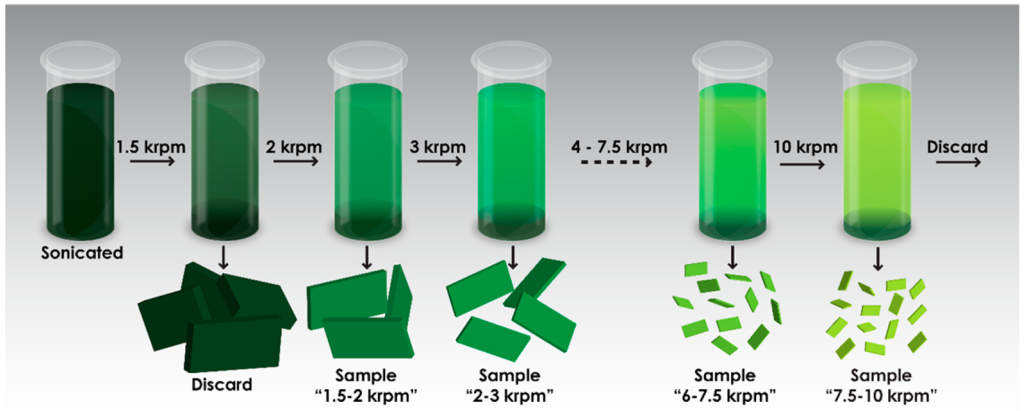

Figure 1. Schematic describing the basic centrifugation cascade employed in this study. The sediment discarded after the first centrifugation contains unexfoliated layered crystallites while the supernatant discarded after the last centrifugation step contains extremely small nanosheets. Size-selected dispersions are prepared by redispersing the collected sediments in 1 g/L aqueous sodium cholate after subsequently increasing centrifugation speeds.

unusual for MoS_2.[15] Such distributions are problematic as many applications require controlled nanosheet sizes: small nanosheets are ideal for catalysis[44] while large ones are needed for mechanical reinforcement.[37] These broad distributions also mean the monolayer content is always low, generally <10%. This is a serious problem for a number of applications. For example, the use of 2D materials in printed optoelectronic devices cannot be considered unless inks containing very high monolayer contents are available.[45] In the longer term, nanosheet printed electronics will require monodisperse suspensions containing only *N*-layers where *N* is defined by the application.

Such capabilities are a long way away. While some progress has been made toward selection of nanosheets by size,[15,43] the available processes are generally inefficient, yielding very small quantities of nanosheets. In addition, monolayer enrichment is much more challenging, not least because the measurement of monolayer content generally involves statistical microscopy which is very time-consuming. While density gradient ultracentrifugation has been used to separate TMD nanosheets by thickness,[46] this procedure is complex, gives low yields (concentrations <0.005 g/L) and is limited to polymer-stabilized dispersions. What is needed is a scalable, universally applicable, high-yield technique to either size-select nanosheets or produce highly monolayer-enriched dispersions. Any such process will involve optimization, which is limited by the tedious microscopic characterization required. Hence, to enable this, it will be necessary to develop fast techniques to measure nanosheet size, thickness and monolayer content. Within this manuscript we address these points.

Inspired by gas-separation centrifugation cascades, we have developed an efficient centrifugation-based method, which allows nanosheet dispersions to be both separated by size and enriched in monolayers in a controlled way. By studying the optical properties of WS_2 dispersions as a function of nanosheet size, thickness and monolayer content, we identified spectral properties which scale with monolayer content as well as mean nanosheet length and thickness, yielding quantitative metrics for these properties. The resultant ability to measure $\langle L \rangle$, $\langle N \rangle$ and monolayer content, allows us to design secondary cascades to further enhance the monolayer content, reaching values as high as 75%. Such monolayer-rich dispersions display easily observable photoluminescence (PL) and optical properties that are distinct from those normally observed for WS_2 ensembles.

RESULTS

Size Selection of WS_2 Nanosheets. As liquid-exfoliated nanosheets tend to be polydisperse in both size and thickness, size selection is almost always required. A number of size-selection techniques exist, mostly based on centrifugation.[3,15,43,46,47] However, these techniques tend to be inefficient, yielding small masses of size-selected nanosheets. To address this, we have developed a new centrifugation-based technique which we denote liquid cascade centrifugation (LCC). We start with a dispersion of liquid-exfoliated nanosheets, obtained by sonication of WS_2 powder in aqueous surfactant solution (see Methods) where any unexfoliated crystallites had been removed by low speed centrifugation (here 1.5 krpm in our centrifuge). This "stock" dispersion contains nanosheets with a broad distribution of sizes and thickness and a small but nontrivial population of monolayers with varying lateral sizes. The stock is then centrifuged at a higher speed (here 2 krpm) and the sediment collected. This sediment contains nanosheets from the larger end of the size distribution and, as they were collected between centrifugation rates of 1.5 and 2 krpm, we refer to this sample as "1.5−2 krpm". Critical to LCC, this sediment can be redispersed[48] completely by mild sonication in H_2O-SC (at SC concentrations as low as 0.1 g/L) to give dispersions with virtually any chosen concentration. The supernatant produced during the 2 krpm centrifugation contains all but the largest nanosheets. It can be centrifuged at a higher rate (here 3 krpm) to give a sediment with slightly smaller nanosheets, which we label "2−3 krpm". The associated supernatant can be centrifuged again and the cascade continued for as many steps as are required with each step using a continually increasing centrifugation rate. Critically, because the heavier, few-layer nanosheets are removed in each step of the cascade, the resultant supernatants become more and more monolayer enriched. After each step, the sediment contains smaller and smaller nanosheets, resulting in effective size selection. Throughout this manuscript, we terminate the cascade at 10 krpm and only partially analyze the final supernatant as it mostly contained free surfactant and extremely small WS_2 nanosheets. This process is illustrated in Figure 1. One very important feature of LCC is that virtually no material

DOI: 10.1021/acsnano.5b07228
ACS Nano XXXX, XXX, XXX−XXX

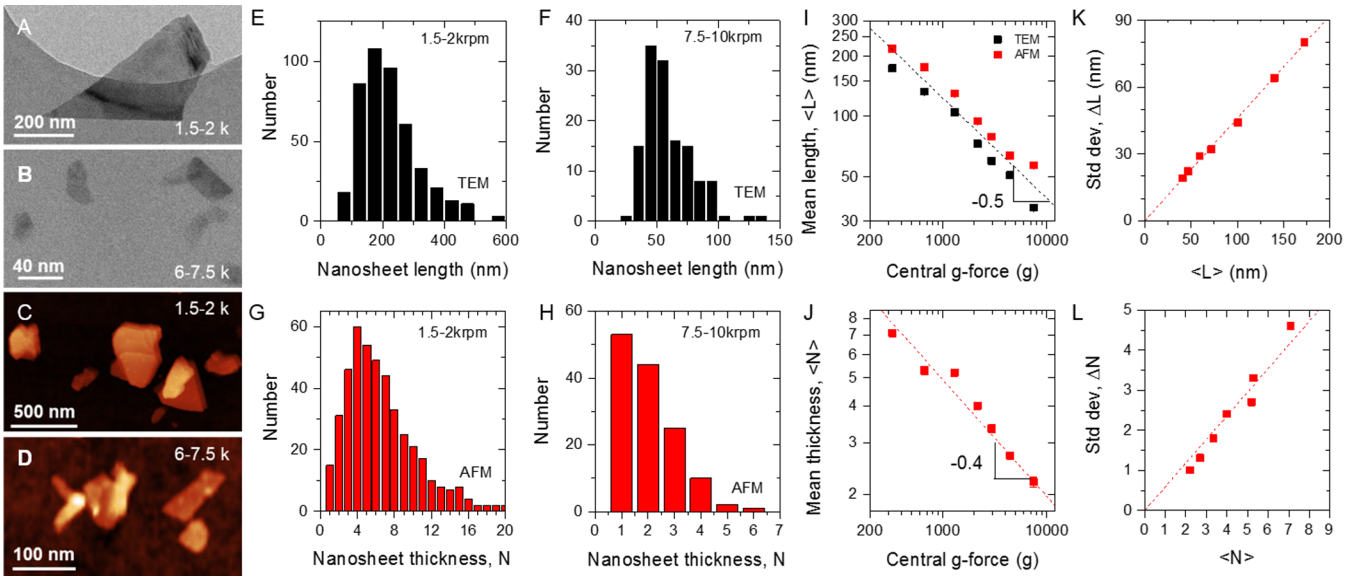

Figure 2. Microscopic characterization of size-selected WS_2 nanosheets. (A–D) TEM (A,B) and AFM (C,D) images of nanosheets, size-selected with upper and lower centrifugation speeds of (A,C) 1.5 krpm and 2 krpm and (B,D) 6 krpm and 7.5 krpm, respectively. (E–J) Statistical analysis of dimensions of nanosheets extracted from images such as those in A–D. This is presented as histograms representing data for lateral nanosheet size measured by TEM (E,F) and nanosheet thickness (number of monolayers per nanosheet, *N*) determined by AFM (G,H). Data is shown for two combinations of centrifugation speed, 1.5–2 krpm and 6–7.5 krpm. (I,J) Data extracted from histograms for a range of centrifugation conditions. Mean values of (I) nanosheet length, $\langle L \rangle$, and (J) nanosheet thickness, $\langle N \rangle$, as a function of the central centrifugation acceleration, presented as central *g*-force. (K,L) Standard deviation of nanosheet length (K) and thickness (L) plotted *versus* mean length and thickness, respectively. The dashed lines in K and L represent $\Delta L/\langle L \rangle = 0.46$ and $\Delta N/\langle N \rangle = 0.59$, respectively.

is wasted, resulting in the collection of relatively large masses of nanosheets in each fraction (see below).

Importantly, the cascade can be designed according to the desired outcome. Here, we wanted to produce a range of dispersions with varying nanosheet sizes and therefore we performed a set of centrifugations with subsequently increasing rpm. However, if only a specific size distribution is desired, the procedure can be simplified by trapping the desired nanosheets between two fixed rpm. For example, if the stock is directly centrifuged at 7.5 krpm and the resultant supernatant then centrifuged at 10 krpm, the collected sediment will contain nanosheets with a size distribution virtually identical to those obtained from the "7.5–10 krpm" step in a cascade. Thus, a cascade can be used when a set of different nanosheet sizes is required but only two centrifugations are required to obtain a single size-selected sample.

We have characterized the nanosheets collected in each fraction microscopically using both transmission electron microscopy (TEM) and atomic force microscopy (AFM) with typical images displayed in Figures 2A–D (see Supplementary Figures S1–S4). In order to characterize the size-selection of LCC, the nanosheet length (*i.e.*, the longest dimension) was measured over all fractions. Example histograms are shown in Figure 2E and 2F for the 1.5–2 krpm and 7.5–10 krpm samples (see Supplementary Figures S1, S4). These histograms show a reduction in nanosheet length as the centrifugation rates are increased (*i.e.*, as the dispersion progresses through the cascade).

Along with nanosheet length and width (defined as the dimension perpendicular to length), the nanosheet thickness, expressed as number of monolayers per nanosheet, *N*, was measured by AFM with the effect of residual surfactant corrected for using step height analysis (SI Figure S5–S6).[9,15,26,31] Typical layer number histograms are shown in Figure 2G,H (see Supplementary Figure S4). Again, we see a reduction in nanosheet thickness as the dispersion progresses through the cascade. Interestingly, the *N* histograms are always log-normal in shape (see SI section 1 1.1–1 1.2) as previously observed for LPE nanosheets.[49]

We can quantify these effects by plotting the mean nanosheet length (measured from TEM and AFM) as a function of the centrifugal acceleration (*g*-force, see Methods) associated with the midpoint of the pair of rpms used in each step of the cascade (see Figure 2I). The mean nanosheet length falls off as $(g\text{-force})^{-0.5}$ as expected due to the close relationship between $\langle L \rangle$ and the "cut size" (*i.e.*, the size of the largest particle remaining dispersed after centrifugation, see Supplementary Figure S7).[21] The lateral dimensions measured by AFM are overestimated due to tip broadening and pixilation effects. The data in Figure 2I has been used to correct the lateral dimensions measured by AFM for the rest of the analysis (see Supplementary Figure S8). We note that we have also analyzed the very small nanosheets that are discarded in the final supernatant of the cascade. TEM (Figure S2) confirms that these are indeed 2D nanosheets with $\langle L \rangle \sim 25$ nm. Because of the small lateral dimensions, a reliable AFM analysis was not possible.

Similarly, the mean nanosheet thickness, $\langle N \rangle$, as measured by AFM is plotted *versus* *g*-force in Figure 2J. The mean number of layers falls with central rotational speed *via* $(g\text{-force})^{-0.4}$. For the set of size-selected samples studied here, it is clear that $\langle L \rangle \propto \langle N \rangle$. This is certainly a limitation of this method as, ideally, one would like to vary $\langle L \rangle$ and $\langle N \rangle$ independently. Below and in the SI (Figure S9) we discuss the relationship between *L* and *N* in more detail. We find the distribution widths (*i.e.*, the standard deviation: ΔL or ΔN) to scale linearly with the mean for both *L* and *N* (see Figures 2K,L) with slopes that are quite high (0.5). This is also not ideal as much smaller values of $\Delta N/$

DOI: 10.1021/acsnano.5b07228
ACS Nano XXXX, XXX, XXX–XXX

$\langle N \rangle$ and $\Delta L/\langle L \rangle$ will be required for most applications. In this work, we have not optimized the procedure to give reduced distribution widths. However, we believe that LCC is versatile enough for such optimization to be achievable.

AFM analysis can also be used to assess the population of monolayers expressed as monolayer number fraction, N_{mono}/N_T. and plotted in Figure 3A as a function of the central *g*-force.

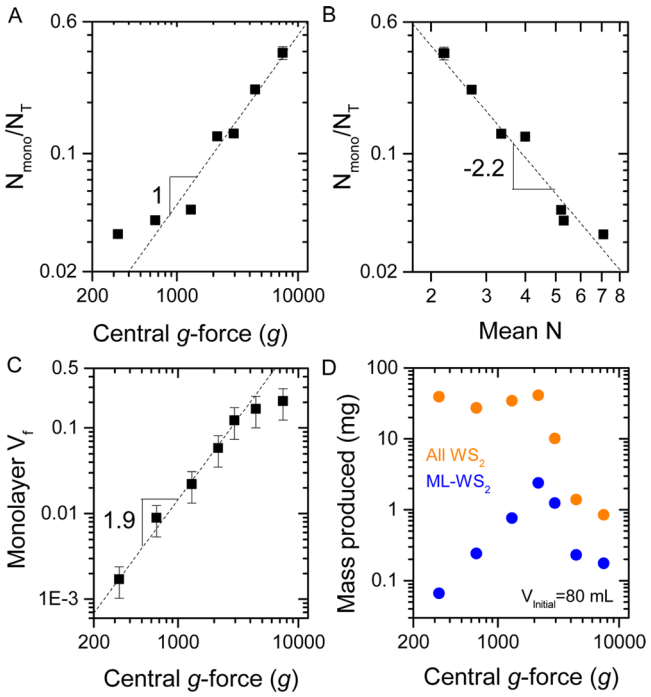

Figure 3. Monolayer population data extracted from statistical AFM for a range of centrifugation conditions. (A) Number fraction of monolayers, N_{mono}/N_T, as a function of the central centrifugal acceleration, presented as *g*-force. (B) Plot of N_{mono}/N_T *versus* mean nanosheet thickness, *N*. (C) Monolayer volume fraction as a function of *g*-force. (D) Total mass of all WS_2 as well as only monolayer-WS_2 produced in each fraction as a function of *g*-force.

Interestingly, we find N_{mono}/N_T to scale linearly with *g*-force as the monolayer content is enriched. After 7 steps in the cascade (*i.e.*, at central acceleration of ~7000*g*), values of N_{mono}/N_T as high as 40% have been achieved. In Figure 3B we plot N_{mono}/N_T *vs* $\langle N \rangle$, finding a very steep fall off, emphasizing the importance in minimizing the mean nanosheet thickness for ML enrichment.

Another way to describe the monolayer content is *via* the monolayer volume fraction, V_f. This has been calculated from the AFM data using the knowledge of nanosheet length, *L*, width, *W*, and thickness, *t* (which we define as $N \times 0.6$ nm) according to eq 1.

$$V_f = \frac{\sum_{mono} LWt}{\sum_{All} LWt} = \frac{\sum_{mono} LW}{\sum_{All} LWN} \quad (1)$$

We find V_f to scale as (*g*-force)$^{1.9}$, reaching ~20% after 7 steps in the cascade (see Figure 3C). Because few-layer nanosheets are typically of higher volume than monolayers, $V_f < N_{mono}/N_T$.

Knowledge of V_f for each fraction is extremely useful as it allows us to assess the mass of ML nanosheets produced in each step once the total WS_2 mass is known. For each step in the cascade, we measured the dispersed WS_2 mass using a combination of weighing and spectroscopy (see Supplementary Figure S10). This data is plotted *versus* central *g*-force in Figure 3D. The stock dispersion (80 mL in volume, ~150 mg of exfoliated WS_2) was separated into 7 fractions with the first four fractions containing 25−40 mg of WS_2 nanosheets each, considerably more than achieved using comparable processes. For example, a multistep centrifugation procedure has reported graphene nanosheet quantities <1 mg[43] while density gradient ultracentrifugation has yielded WS_2 monolayer-rich dispersions with concentrations of <0.005 g/L.[46]

However, after the fourth step in the cascade, (*i.e.*, for central *g*-forces above ~2000*g*) the mass produced falls off sharply, reaching ~1 mg after step 7 (~7000*g*). The mass of monolayers produced is related to the total WS_2 mass by $M_{ML} = V_f M_T$ allowing us to calculate the mass of monolayers as also plotted *versus* central *g*-force in Figure 3D. We find the monolayer mass to increase over the first 4 steps of the cascade as the dispersions become more and more enriched. However, even though enrichment continues in subsequent steps, it falls off after step 4 as the total dispersed mass declines. This data clearly shows that highly enriched samples can be achieved by collecting nanosheets using high centrifugation rates but at the cost of low yield. Alternatively, the mass of monolayers collected can be optimized by using midrange centrifugation rates.

Relationship between Nanosheet Length and Thickness. The data in Figure 1I,J shows the mean nanosheet length and thickness of the different samples to be in proportion to each other. However, this hides important trends within each sample. Shown in Supplementary Figure S9A is a plot of *L* *versus* *N* measured for all individual nanosheets over the seven samples prepared in the cascade described above. While this graph appears to be consistent with the proportionality of *L* and *N*, closer inspection shows that, for a given sample (*e.g.*, 4−6 krpm as shown in inset), the nanosheet length does not vary systematically with thickness. To investigate this more carefully, we extracted the mean nanosheet length for each value of *N*, which we plotted *versus* *N* for each sample in Figure S9B. This shows that for a given step in the cascade, the mean nanosheet length is roughly independent of N: *e.g.*, for the 7.5−10 krpm sample, the mean monolayer length is 41 nm while the mean 4-layer length is 45 nm. This implies that the separation mechanism predominately involves nanosheet length rather than mass as might be expected. However, lower central *g*-forces result in larger nanosheets in general and so larger monolayers. For the relatively low central *g*-forces (2−3 krpm sample) the mean monolayer length was as high as 130 nm with individual monolayers as long as 200 nm observed. Unfortunately, because these large monolayers are found in the low *g*-force samples, they tend to be relatively rare. To date we have not found a way to highly enrich a sample with long monolayers rather than the shorter (~50 nm) monolayers found in the 7.5−10 krpm sample. We note that monolayer length distribution in the stock is probably set by the exfoliation conditions (*e.g.*, details of sonication regime and stabilizer). In the future, it would be useful to identify conditions which would give a much larger initial population of large monolayers.

Dependence of the Optical Extinction Spectra on the Nanosheet Dimensions. It has previously been shown in the case of liquid-exfoliated MoS_2, that the spectral profile of optical extinction (or absorbance) spectra strongly depends on nanosheets dimensions due to edge and confinement effects.[15] Here we use the fractions produced by LCC to investigate the

DOI: 10.1021/acsnano.5b07228
ACS Nano XXXX, XXX, XXX−XXX

effect of nanosheet size and thickness on the optical properties of LPE WS_2.

To do this, we first measured the optical extinction spectra for the fractions described above (*N.B.*, the extinction, *Ext*, is related to the transmittance, *T*, by $T = 10^{-Ext}$ and to the extinction coefficient, ε, by $Ext = \varepsilon Cl$ where *C* is the nanosheet concentration and *l* is the cell length). The extinction coefficients were calculated using the measured mass of dispersed nanosheets (see Supplementary Figure S10). As shown in Figure 4A, optical extinction spectra of liquid-exfoliated WS_2, display the characteristic excitonic transitions,[27]

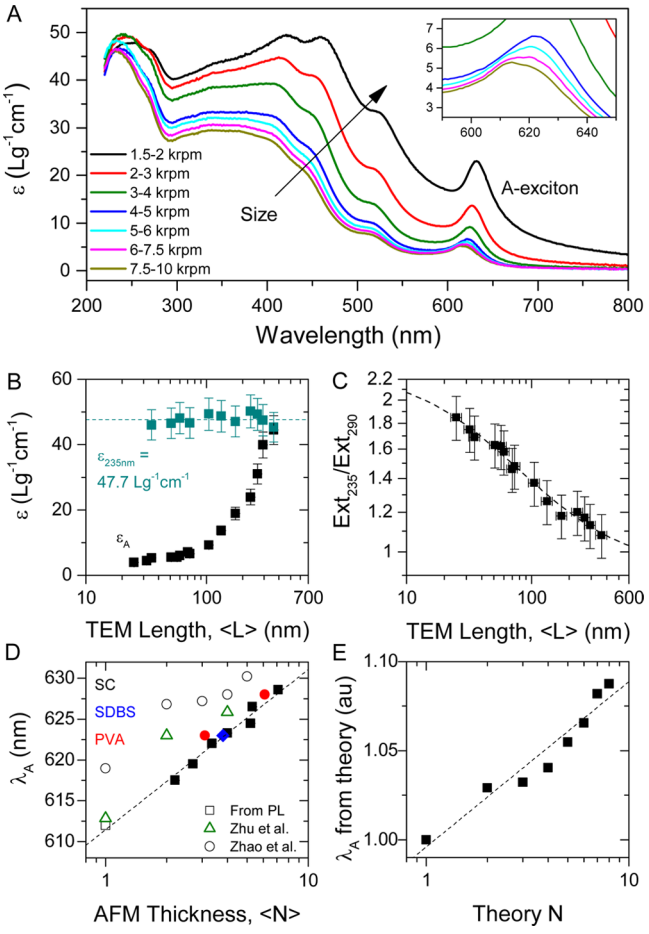

Figure 4. Dependence of the optical properties of nanosheet dispersions on the nanosheet dimensions. (A) Optical extinction coefficient spectra measured for WS_2 dispersions (water/SC) prepared using different centrifugation conditions, and so with different mean nanosheet lengths and thicknesses. Inset: magnified A-exciton region. (B) Extinction coefficient, measured at 235 nm and at the A-exciton position (~615 nm) plotted *versus* mean nanosheet length, as measured by TEM. The mean value of ε_{235} is 47.7 Lg^{1-} cm^{-1}. (C) Ratio of extinction at 235 nm to that at 290 nm plotted *versus* mean nanosheet length, as measured by TEM. The dashed line is a fit to eq 2. (D) A-exciton center of mass position (determined from second derivatives) plotted *versus* mean nanosheet thickness. Also included is data for WS_2 nanosheets dispersed in SDBS and PVA and from the literature.[51,52] The open symbol represents the A-exciton position from photoluminescence measurements. The dashed line shows an empirical relationship between λ_A and *N* according to eq 4. (E) Calculated relative wavelength associated with the optical gap of WS_2 (*i.e.*, the direct band gap at the K-point).

but vary systematically with nanosheet size and thickness due to edge and confinement effects.[15] Similar behavior is observed for the absorbance and scattering coefficient spectra (see Supplementary Figure S11).[15] Importantly, the scattering coefficients are relatively small for these nanosheets, meaning that the absorbance and extinction are very similar. The edge effects result in a dependence of the spectral profile on nanosheet length. As a result the extinction coefficient, for example at the A-exciton (~620 nm), depends strongly on nanosheet length as shown in Figure 4B. However, the extinction coefficient at 235 nm is invariant with nanosheet length ($\varepsilon_{235\ nm}$ = 47.7 Lg^{1-} cm^{-1}), allowing its universal use to measure the concentration of WS_2.

The effect of edges on the spectral shape can be quantified *via* the ratio of extinction intensities at two different wavelengths, *e.g.*, at 235 nm to that at 290 nm, Ext_{235}/Ext_{290}, which is plotted in Figure 4C. Similar to MoS_2, the data in Figure 4C can be fitted to the following equation[15]

$$\frac{Ext_{235}}{Ext_{290}} = \frac{\alpha_C(235\ \text{nm})L + 2x(k+1)\Delta\alpha(235\ \text{nm})}{\alpha_C(290\ \text{nm})L + 2x(k+1)\Delta\alpha(290\ \text{nm})} \quad (2)$$

where α_C is the absorption coefficient associated with the nanosheet basal plane, $\Delta\alpha = \alpha_E - \alpha_C$ where α_E is the edge region absorption coefficient, and *L*, *x* and *k* are the nanosheet length, edge thickness and aspect ratio, respectively.[15] We find this equation fits the data very well allowing us to generate a function which relates the mean nanosheet length, *L* to the extinction peak intensity ratio:

$$L(\text{nm}) = \frac{2.3 - Ext_{235}/Ext_{290}}{0.02Ext_{235}/Ext_{290} - 0.0185} \quad (3)$$

This relationship is extremely useful as it allows the mean nanosheet length in any dispersion to be extracted from an extinction spectrum. Other peak intensity ratios yield similar relationships as discussed in the SI (see Supplementary Figure S12).

In addition, the extinction spectra also contain information on mean nanosheet thickness due to confinement effects. These result in shifts of the A-exciton position (see Figure 4A inset) toward lower wavelengths as the nanosheet thickness is reduced. Interestingly, for the 7.5−10 krpm sample, previously unseen structure begins to appear with a peak at ~612 nm and a shoulder at ~622 nm. The origin of this will be discussed in more detail below.

The relationship between the center of mass position of the A-exciton, λ_A, (determined from the second derivative of the A-exciton, Supplementary Figure S13) and the mean WS_2 nanosheet thickness is displayed in Figure 4D. As with MoS_2, λ_A increases logarithmically with nanosheet thickness.[15] We find data for WS_2 exfoliated in sodium dodecylbenzenesulfonate (SDBS) and poly(vinyl alcohol) (PVA) to sit very close to the same line suggesting solvatochromic effects to be small (but not nonexistent, see SI).[50]

In any case, fitting the data in Figure 4D to an empirical relation gives an equation, which allows us to extract the mean nanosheet thickness from the wavelength associated with the A-exciton:

$$\langle N \rangle = 6.35 \times 10^{-32} e^{\lambda_A(\text{nm})/8.51} \quad (4)$$

This equation is at least applicable to aqueous SC-, SDBS- and PVA-stabilized WS_2 dispersions and almost certainly gives

DOI: 10.1021/acsnano.5b07228
ACS Nano XXXX, XXX, XXX−XXX

approximate nanosheet thicknesses in a wide range of liquid environments (see below and SI).

Because these shifts in A-exciton position will become important later in the paper, we need to verify this behavior as much as possible. We found similar trends had been observed by Zhu *et al.* and Zhao *et al.* for absorbance/reflectance spectra of micromechanically cleaved WS_2.[51,52] We note that the literature data from micromechanically cleaved WS_2 is offset to lower energies compared to our data presumably to the different dielectric environment.[50,53] In addition, we have attempted to confirm these effects by calculating the electronic band structure of WS_2 nanosheets as a function of *N*. As shown in Figure 4E, the computed direct transition at the K-point (see Methods) of the Brillouin zone follows a similar logarithmic dependence on layer number as observed in the experimental data.

It is worth noting that eqs 3 and 4 might only be expected to hold for surfactant exfoliated WS_2 nanosheets. To test this we performed a cascade for WS_2 nanosheets exfoliated in the solvent *N*-methyl-pyrrolidone (NMP).[4] We found the length metric described by eq 3 to apply very well to NMP-exfoliated WS_2. However, we observed a small degree of solvatochromism which resulted in shifts in λ_A due to environmental effects (~1.5 nm shift between NMP- and SC-stabilized nanosheets). This means that although eq 4 can be used to approximately find nanosheet thicknesses from extinction spectra of NMP-based dispersions, slight modifications are required to accurately extract nanosheet thicknesses in NMP. This modified metric is given in Figure S23.

Dependence of the Photoluminescence on the Monolayer Content in the Dispersions. While quantitative spectroscopic metrics for length and thickness are instructive, a metric for ML content would be even more useful. The most obvious candidate is the nanosheet photoluminescence (PL) as this is only appreciable in monolayers for the common group VI-TMDs.[51,54−56] However, previous experiments on MoS_2 dispersions showed that PL can only be detected using standard luminescence spectrometers for dispersions with high monolayer content,[15] making routine PL characterization impossible.

Here we use the superior sensitivity of a Raman spectrometer to detect PL even in noncentrifuged stock dispersions with low ML content. We found that, when acquiring a Raman spectrum from the surface of liquid drops (λ_{exc} = 532 nm), the photoluminescence of the monolayer is typically detected at high wavenumbers (~2460 cm^{-1}). *N.B.*, the measurement has to be carried out with extreme care (see Methods). The Raman/PL spectra normalized to the WS_2 2LA(M) Raman mode (355 cm^{-1}, 543 nm) of size-selected WS_2 nanosheet dispersions are plotted in Figure 5A as a function of wavelength (also compare Figure S14). The WS_2 Raman modes plotted *versus* wavenumber are shown in the inset. In addition to the WS_2 Raman modes, in all cases, the typical photoluminescence peak of the WS_2 is detected at ~612 nm (the feature at ~650 nm is the Raman response of water).

A typical PL spectrum measured in this way is plotted *versus* photon energy in Figure 5B. All spectra fit reasonably well to single Lorentzians, representing excitonic emission. While we initially expected inhomogeneous broadening to render Gaussian fitting more appropriate, we consistently found more reliable fits using Lorentzians (see Supplementary Figure S15). The Lorentzian is centered at 2.023 eV invariant of centrifugation conditions (see Figure 5C inset). However, as

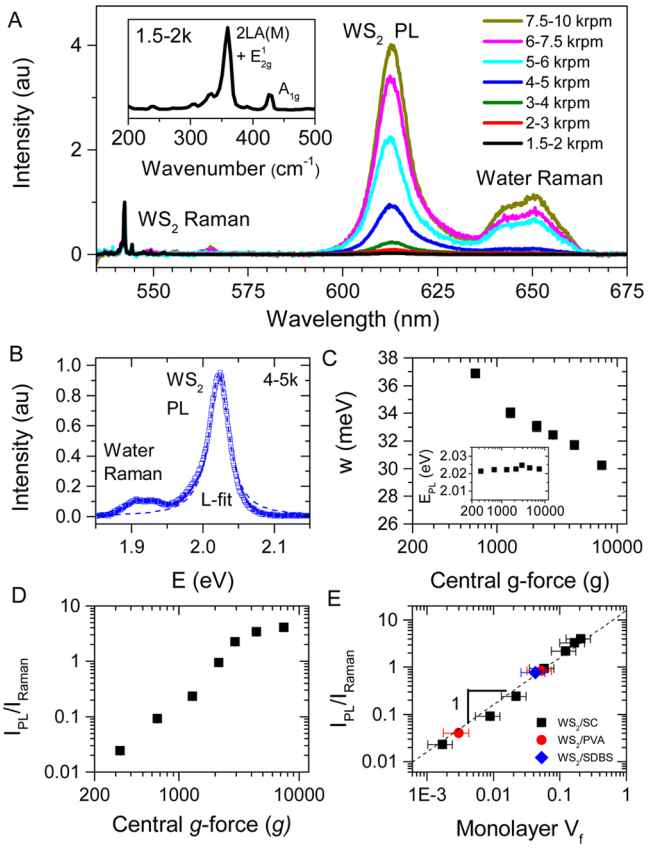

Figure 5. Photoluminescence data for dispersions with different monolayer content. (A) Photoluminescence (~610 nm) and Raman (~540 nm) spectra of surfactant-stabilized WS_2 dispersions prepared with different centrifugation conditions and measured in liquid using a Raman spectrometer (λ_{exc} = 532 nm). The spectra were normalized to the 2LA(M) Raman mode of WS_2. The feature at ~650 nm is the water Raman peak. Inset: Raman spectrum of dispersed WS_2 nanosheets plotted *versus* wavenumber. (B) Photoluminescence spectrum of WS_2, plotted on an energy scale and fitted to a Lorentzian. (C) PL line width, from Lorentzian fits, plotted *versus* central centrifugation acceleration (expressed in units of *g*). Inset: PL position *vs* *g*-force. (D) Ratio of PL intensity to Raman intensity, I_{PL}/I_{Raman}, plotted *vs* *g*-force. E) I_{PL}/I_{Raman} plotted *versus* monolayer volume fraction. The dashed line represents $I_{PL}/I_{Raman} = 17 \times V_f$.

shown in Figure 5C, the line width appears to fall off with increasing centrifugation rate suggesting larger nanosheets to be slightly more defective than smaller ones. It must be noted that these PL peaks are very narrow, displaying widths as low as 30 meV. WS_2 usually displays PL line widths between 22 and 75 meV,[51,57] with the lower values found only on nonperturbing surfaces like BN. This suggests that, not only does the water/SC environment not significantly dope the nanosheets, but also that they are largely defect-free (see Supplementary Figure S16).

As shown in Figure 5D, we found the ratio of PL to Raman intensity to increase strongly with central *g*-force as the monolayer population increases. This suggests that this intensity ratio, I_{PL}/I_{Raman}, can be quantitatively linked to the monolayer content. We propose that the intensity of the Raman spectrum is proportional to the total number of WS_2 formula units probed by the laser. However, because only the monolayers are luminescent, the PL intensity should be proportional to only the WS_2 formula units associated with

DOI: 10.1021/acsnano.5b07228
ACS Nano XXXX, XXX, XXX−XXX

monolayers. This implies that I_{PL}/I_{Raman} should scale linearly with the monolayer volume fraction. To test this, in Figure 5E we plot I_{PL}/I_{Raman} *versus* the monolayer volume fraction, V_f, (as measured by AFM, Figure 3C). We find a linear relationship which holds over >2 decades of both I_{PL}/I_{Raman} and V_f. Interestingly, equivalent measurements for WS_2 nanosheets exfoliated in SDBS and PVA give data which falls on the same curve strongly suggesting that this metric is quite robust toward changes in the stabilizer, although it may depend on the quality of the WS_2 starting material. To further test the robustness of this metric, as well as the metrics based on UV−vis spectroscopy, we have redispersed WS_2 size-selected by LCC in SC of varying concentrations from 0 to 5 g/L. As shown in Figures S17−18, spectra and hence the results of the metric analysis do not change as a function of stabilizer concentration. In addition, this shows that the LCC size-selected WS_2 can even be redispersed in water without aggregation occurring immediately.

From the fit line in Figure 5E, we find

$$V_f = \frac{1}{17}\frac{I_{PL}}{I_{Raman}} \quad (5)$$

This relationship holds over a broad range of sizes and monolayer contents, but we note that it eventually breaks down for very small nanosheets, as edges may activate nonradiative decay. A first indication that this is indeed the case is obtained from an analysis of the very small nanosheets that are discarded in the supernatant after centrifuging at 10 krpm (see SI Figure S14, $\langle L \rangle \sim 25$ nm). While TEM and optical extinction show no obvious deviation from larger nanosheets, the PL/Raman ratio is significantly lower than in the 7.5−10 krpm sample suggesting edge effects to play a role. This issue is addressed further in the Supporting Information.

Nonetheless, this is an important result, as it means that the monolayer volume fraction in a dispersion of WS_2 nanosheets can be quantified very simply and easily from a Raman/PL measurement. This is hugely advantageous over traditional techniques such as AFM or TEM, which are very time-consuming and can require skill and experience from the experimenter. Critically, it allows us to track the monolayer content as we perform further monolayer enrichment as described below.

Optical Properties of Dispersions Highly Enriched in Monolayers. In the preceding sections we described a very simple primary centrifugation cascade which resulted in the production of a range of size-selected fractions at much higher yields than homogeneous centrifugation (see Supplementary Figure S19), the last of which was monolayer-enriched up to $N_{mono}/N_T \sim 40\%$ and $V_f \sim 20\%$. However, the strength of LCC is its versatility. For example, it is also applicable to nanosheets exfoliated in solvents (see SI Figures S20−23). In addition, much more complex cascades can be designed, resulting in higher degrees of monolayer enrichment. For example, we find the monolayer content to rise rapidly with iteration cycle when repeating the centrifugation at fixed rpm (see Supplementary Figure S24).

In the following, we used the ability to spectroscopically measure the volume fraction of monolayers to design secondary cascades with the goal of maximizing I_{PL}/I_{Raman}. Details are presented in the Supporting Information (see Supplementary Figures S25−38). In brief, we designed centrifugation protocols for monolayer enrichment consisting of multiple iterations starting from size-selected dispersions. These typically involved centrifugation at relatively low speeds and longer times (overnight) to remove few-layered WS_2 and centrifugation at high speeds and short times (1−4 h) to remove very small nanosheets (see Supplementary Figure S25). We note that when designing such a cascade, if highly luminescent dispersions are required, the small-nanosheet-removal step is crucial as we found PL/Raman ratios to be significantly lower for very small nanosheets even at high ML contents, probably due to edge effects (see Supplementary Figures S33−S34).

Below we will describe secondary cascades (S.C.), which used strongly (primary sample 6−8 krpm, secondary sample labeled S.C.1, Figure S26−28) and weakly (1.5−10 krpm, S.C.2, Figure S29−31) size-selected dispersions as starting points for monolayer enrichment. Shown in Figure 6A is an AFM layer number histogram for the S.C.2 dispersion with a typical image in the inset. It is clear that this sample is dominated by monolayers with AFM analysis giving $N_{mono}/N_T \sim 74\%$ and $V_f \sim 70\%$ (see Table 1 for all monolayer content data). The Raman/PL spectra of the 6−8 krpm dispersion and both ML enriched dispersions are shown in Figure 6B. While the 6−8 krpm dispersion displayed $I_{PL}/I_{Raman} = 2.8$, equivalent to $V_f = 0.16$, it is clear that the enriched samples display considerably more intense PL. We found $I_{PL}/I_{Raman} = 10.9$ and 12.7, for the S.C.1 and S.C.2 dispersions, giving V_f of 65% and 75%, respectively, in good agreement with AFM statistics (Table 1).

Shown in Figure 6C are extinction spectra for both the 6−8 krpm sample and the S.C.1 and S.C.2 dispersions. The shapes of these spectra are almost indistinguishable because high speed centrifugation steps have been included in the cascade to remove very small nanosheets giving similar $\langle L \rangle$ values for these dispersions (confirmed by AFM statistics, see Supplementary Figure S28). We note that in this nanosheet size range, scattering[15] is virtually nonexistent so the extinction spectrum is identical to the absorbance spectrum (see Supplementary Figure S32).

However, much more interesting is the shape of the A-excitonic components of the extinction spectra as shown in the inset of Figures 4A and 6C. These show changes not only in center of mass peak position but also in shape. Unlike the spectra associated with thicker nanosheets, the 6−8 krpm spectrum clearly has a peak at ∼612 nm and a shoulder at ∼622 nm as discussed above (see Figure 4A). However, the ML-rich samples clearly have A-excitonic responses, which are dominated by a peak close to 610 nm (2.032 eV). This is extremely close to the position of the A-excitonic PL peak (2.023 eV, implying a Stokes shift of 10 meV). Thus, we associate the feature at ∼610 nm in the extinction/absorbance spectrum of the ML-rich sample with the absorbance of monolayer WS_2. This suggests the component at ∼622 nm represents the combined contribution of few-layered WS_2.

To test this in more detail, we carefully smoothed the extinction spectra of all samples (see SI section 7) before finding the second derivative with respect to energy, $d^2(Ext)/dE^2$. Such a procedure is known to narrow contributing peaks roughly 3-fold, allowing resolution of closely spaced peaks.[58] Examples of the resultant second derivatives are shown in Figure 6D. Monolayer-poor samples such as 1.5−2 krpm are dominated by one peak at ∼1.98 eV while the monolayer-rich sample (S.C.1) is dominated by one peak at ∼2.03 eV, with intermediate samples showing both components.

DOI: 10.1021/acsnano.5b07228
ACS Nano XXXX, XXX, XXX−XXX

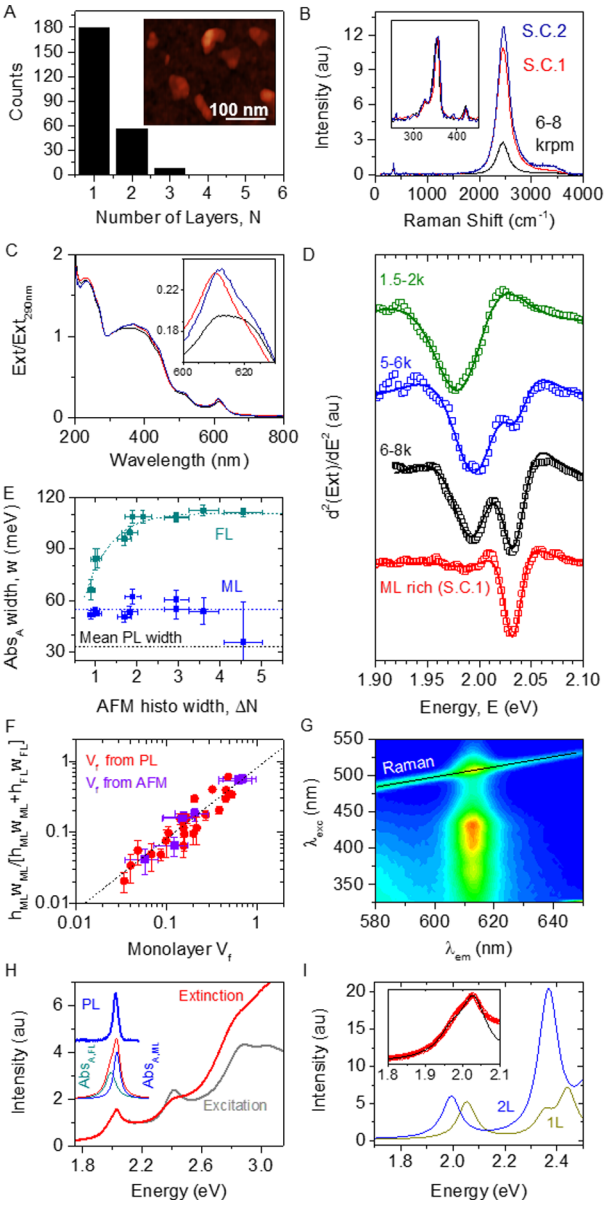

Figure 6. Characterization of second stage monolayer enriched dispersions. (A) AFM nanosheet thickness (expressed as layer number) histogram and representative image of WS_2 nanosheets from a dispersion enriched in monolayers by a secondary LCC. (B) Raman/PL spectra of the ML-rich dispersion (red) compared to the first stage size-selected dispersion used for the ML enrichment centrifugation (blue). An alternative secondary cascade yielded a similar dispersion (yellow). (C) Optical extinction spectra of the three dispersion. Inset: Zoom in of the A-exciton showing clear changes in spectral shape. (D) Second derivative spectra for a number of WS_2−SC dispersions fitted to the sum of the second derivatives of two Lorentzians. With increasing ML volume fraction, a well separated component at 2.033(3) eV (~610 nm) can clearly be identified which is attributed to ML-WS_2. (E) Width of absorbance Lorentzian curves, representing mono- and few-layer nanosheets, found by fitting second derivatives such as those shown in D plotted *versus* the full width at half-maximum of the corresponding AFM thickness histogram. Shown for comparison is the mean width of the PL spectra in Figure 5A. (F) A-exciton shape monolayer metric, obtained from fitting the second derivative of the extinction spectra to two Lorentzians, as a function of ML volume fraction. The violet squares represent data where V_f was measured from AFM, whereas V_f was determined from the PL/Raman ML metric in the case of the red data points. The dashed line shows a linear relation that can be used to determine the V_f from the shape of the A exciton according to eq 8. (G) Excitation−emission contour plot of the ML-rich dispersion measured in a PL spectrometer. (H) Extinction spectrum of the ML-rich dispersion compared to the excitation spectrum at the ML emission (after subtraction of the water background). The same excitonic features are evident in both spectra. Lower inset: A-exciton absorbance deconvoluted into the individual components of ML and few-layer WS_2 as well as their sum. Upper inset: Measured PL spectrum (450 nm excitation). (I) Theoretical absorption curves for monolayer (1L) and bilayer (2L) WS_2. Inset: Extinction curve measured for S.C.2 monolayer enriched sample (open symbols). Also shown is the weighted sum ($Abs = 0.71Abs_{1L} + 0.24Abs_{2L}$, black line) of the theoretical monolayer and bilayer absorption spectrum. These weightings were chosen to reflect the volume fraction of monolayers and bilayers in the S.C.2 sample as measured by AFM (see A) where we have neglected the small population of trilayers for simplicity. *N.B.*, the theory curve has been downshifted to 25 meV to match the experimental data.

Table 1. Summary of Data Relating to Monolayer Content for Size-Selected Starting Dispersions and Dispersions Enriched by Secondary Cascades

sample	$\langle N \rangle$	N_{mono}/N_T	V_f	I_{PL}/I_{Raman}
6−8 krpm	2.4	0.30	0.15	2.7
S.C.1	1.6	0.73	0.64	10.8
1.5−10 krpm	9.0	0.04	0.01	0.18
S.C.2	1.6	0.74	0.70	12.7

We can extract more information about the components by fitting the second derivatives. In the simplest form, a Lorentzian line can be described by

$$L(E) = \frac{h}{\left[1 + \left(\frac{(E - E_0)}{w/2}\right)^2\right]} \quad (6)$$

where h represents the height, E_0 the center and w the fwhm. As described in the SI (see SI section 7), we have fit the second derivative curves to the sum of two doubly differentiated Lorentzians, allowing us to extract height, width and position for both (see Supplementary eq S10 and Figure S39). As before, Lorentzians gave better fits than Gaussians (see Figures S40−S41). We find extremely good fits in all cases (see solid lines in Figure 6D). The higher energy component always had a position of E_0 = 2.035 eV consistent with it representing absorbance of the monolayer A-exciton. The lower energy component was found between 1.98 and 1.997 eV. We associate this component with the individually unresolvable sum of few-layer A-exciton absorptions. In fact, the monolayer component can be differentiated from the few-layers only because of the logarithmic dependence embodied in eq 4. This equation implies that the energy difference between A-excitonic transitions for 1- and 2- layer nanosheets is 19 meV while being only 11 meV between 2- and 3-layer nanosheets and 8 meV between 3- and 4-layer nanosheets.

If the mono- and few-layer assignment described above is correct, then we expect the width of the monolayer A-exciton absorbance peak to be invariant with the width of the nanosheet thickness distribution. Conversely, the width of the few-layer A-exciton absorbance peak should increase as the

DOI: 10.1021/acsnano.5b07228
ACS Nano XXXX, XXX, XXX−XXX

thickness distribution broadens. This is exactly what we observed as plotted in Figure 6E (the lines are guides to the eye). The FL peak width increases from ~65 to ~110 meV as the AFM thickness histogram width increases from 1 to 4.5. Conversely the monolayer peak is always ~55 meV wide. Interestingly this is almost twice as wide as the PL peak. This likely partly stems from the fact that all monolayered nanosheets are probed in absorbance, while the smallest nanosheets are not captured in the PL measurement (see Supplementary Figures S33–S34).

With this peak assignment in mind, we propose that the area under the ML A-exciton extinction peak should scale with the monolayer content in the dispersion. Because the area under any Lorentzian is proportional to $h \times w$, we have calculated the metric S_A:

$$S_A = \frac{h_{ML} w_{ML}}{h_{ML} w_{ML} + h_{FL} w_{FL}} \quad (7)$$

which we suggest should scale with the monolayer volume fraction. We have plotted S_A *versus* V_f in Figure 6F, finding good linearity as described by $S_A = (0.8 \pm 0.05) V_f$. The fact that the proportionality constant is so close to 1 is a strong indicator that our assignment is correct. This allows us to use S_A as an alternative metric for the monolayer volume fraction:

$$V_f = (1.25 \pm 0.08) S_A \quad (8)$$

The availability of highly monolayer-enriched dispersions allows us to measure the photoluminescence using a standard PL spectrometer exciting with Xe lamp to obtain excitation emission contour plots as shown in Figure 6G. Emission from the A-exciton can be well resolved with fitting of the emission spectrum (see Supplementary Figure S32) giving position and widths virtually identical to those measured in the Raman spectrometer.

The real advantage of measurement with the PL spectrometer is the ability to measure excitation spectra. Such spectra generally allow the measurement of the absorption spectrum of the luminescent species at higher resolution than would usually be possible. As shown in Figure 6H, the measured excitation spectrum (λ_{em} = 617 nm) shows the same spectral features as the extinction spectrum. However, these features, which can be attributed to B, C and D excitonic transitions, are considerably sharper in the excitation spectrum. As an inset in Figure 6I, we also compare the measured PL spectrum with the deconvoluted A-exciton absorbance contributions from mono- and few-layer WS_2 (calculated from the second derivative fit parameters). The monolayer A-exciton absorbance is very close to the PL with only a slight Stokes shift (~10 meV).

To test our understanding of this behavior, we have used *ab initio* GW plus Bethe-Salpeter method to calculate the absorption spectrum of both mono- and bilayer WS_2 as shown in Figure 6I (see Methods). We find a strong dependence on layer number with the A-exciton shifting from 2.06 eV for the ML to 1.99 eV in the bilayer in reasonable agreement with the data in Figure 4D. We can model the absorption spectrum of a monolayer rich dispersion (S.C.2) by calculating the weighted average of the theoretical mono- and bilayer spectra where the weighting factors are the measured mono- and bilayer volume fractions (see Figure 6A, we ignore the small trilayer population for simplicity). We find excellent agreement between measured and calculated spectra in the A-exciton regime once the calculated spectra have been normalized and downshifted by 25 meV. We attribute the shift to a combination of environmental and temperature effects.

CONCLUSION

Liquid cascade centrifugation is a simple, powerful and broadly applicable technique to separate liquid exfoliated nanosheets by size. It has a number of advantages over other techniques; notably its high yield and lack of wastage; the ability to control the concentration of size-selected suspensions, even up to very high concentrations. Probably most important is its versatility: cascades can be designed to produce the desired size and thickness distributions and the required degree of monolayer enrichment. Ultimately, we believe cascades will be designed to produce dispersions containing only a given nanosheet thickness at a predetermined lateral size. In addition, this technique can be applied to virtually any 2D material stabilized by solvents, surfactants or polymers using only benchtop centrifuges.

The ability to easily size-select nanosheets has enabled us to study their optical properties as a function of size and thickness. Similar to MoS_2,[15] we found the extinction spectra of WS_2 suspensions to contain quantitative information describing both mean length and thickness of the nanosheets while the PL spectra quantify the monolayer content. Spectroscopic measurement of size, thickness and monolayer content allows cascade design to achieve further monolayer enrichment, enabling the study of the fundamental optical properties of nanosheet ensembles. For example, once the monolayer content was increased beyond $N_{mono}/N_T \sim 25\%$, fine structure began to appear in the extinction spectra in the vicinity of the A-exciton. We found it possible to differentiate the contributions to A-exciton extinction of mono- and few-layer nanosheets allowing us to use a simple extinction spectrum to measure the monolayer content of a suspension.

We believe that the ability to easily size select and monolayer enrich dispersions, coupled with the availability of quantitative spectroscopic metrics to assess mean nanosheet length, thickness and monolayer volume fraction will have impact for both applications and fundamental studies. Nanosheet sizes and thicknesses will be precisely tailored according to needs in samples, which will be available in large quantities. This will be especially critical for applications such as printed electronics where dispersions of electronically identical, and so uniformly sized, nanosheets are required. Optical analysis will become a tool for quality control allowing the concentration, size, thickness and monolayer content to be assessed for any dispersion. In addition, PL will be used as a fingerprint, which is sensitive to doping and environmental effects allowing an *in situ* probe for intermolecular interactions.

METHODS

Sample Preparation. WS_2 dispersions were prepared by probe sonicating the powder. WS_2 (20 g/L) was immersed in 80 mL of aqueous surfactant solution (C_{surf} = 6g/L). The mixture was sonicated under ice-cooling in a metal beaker by probe sonication using a solid flathead tip (Sonics VX-750) for 1 h at 60% amplitude. The dispersion was centrifuged in a Hettich Mikro 220R centrifuge equipped with a fixed-angle rotor 1016 at 5 krpm (2660*g*) for 1.5 h. The supernatant was discarded and the sediment collected in 80 mL of fresh surfactant and subjected to a second sonication 5 h at 60% amplitude with a pulse of 6 s on and 2 s off.

DOI: 10.1021/acsnano.5b07228
ACS Nano XXXX, XXX, XXX–XXX

To select nanosheets by size, we used controlled centrifugation with sequentially increasing rotation speeds. Two different rotors were used (see SI). In the standard primary cascade, unexfoliated WS_2 was removed by centrifugation at 1.5 krpm (240*g*, 2 h). The supernatant was subjected to further centrifugation at 2 krpm (426*g*, 2 h). The sediment was collected in fresh surfactant at reduced volume (3−8 mL), while the supernatant was centrifuged at 3 krpm (958 g, 2 h). Again, the sediment was collected and the supernatant subjected to centrifugation at higher speeds. This procedure was repeated with the following speeds: 4 krpm (1700*g*, 2 h), 5 krpm (2660*g*, 2 h), 6 krpm (3506*g*, 2 h), 7.5 krpm (5480*g*, 2 h), 10 krpm (9740*g*, 2 h). The data presented in Figure 1 uses the central rpm/*g*-force to express the consecutive centrifugation. For example, the sediment collected from the centrifugation between 2 and 3 krpm has a central rpm of 2.5 krpm (665*g*).

To perform the monolayer enrichment, a sample size-selected by the standard procedure was subjected to further iterative centrifugation steps. Details are described in Section 6 of the Supporting Information. The sample of S.C.1 shown in Figure 6 was produced from a standard size selection between 6 and 8 krpm. The dispersion was then centrifuged at 4 krpm (1560*g*) for 6 h. the sediment was discarded and the supernatant centrifuged at 5 krpm (2435*g*) for 14 h. The sediment was discarded and the supernatant centrifuged at 9 krpm (7890*g*, 4 h). Very small nanosheets were removed in the supernatant after further centrifugation at 15 krpm (21915*g*, 1 h). Alternatively, for S.C.2 a dispersion containing nanosheets sedimenting between 1.5 and 10 krpm was centrifuged as follows: 2.5 krpm (609*g*, 16 h), supernatant subjected to 4 krpm (1560*g*, 14 h), supernatant subjected to 10 krpm (9740*g*, 1 h), sediment collected in 1.5 mL and subjected to 5 krpm (2436*g*, 5 h), supernatant subjected to 8 krpm (6235*g*, 2 h), sediment collected and subjected to 3 krpm (877*g*, 12 h). The supernatant after this last centrifugation step was collected and had a monolayer volume fraction of ∼70−75%.

Characterization. Optical extinction was measured on a Varian Cary 500 in quartz cuvettes in 1 nm increments. Bright field transmission electron microscopy imaging on Holey carbon grids (400 mesh) was performed using a JEOL 2100, operated at 200 kV. Statistical analysis was performed of the flake dimensions by measuring the longest axis of the nanosheet and assigning it "length" and the dimension perpendicular to the longest axis which we defined as "width". Atomic force microscopy (AFM) was carried out on a Veeco Nanoscope-IIIa (Digital Instruments) system in tapping mode after depositing a drop of the dispersion (10 μL) on a preheated (150 °C) Si/SiO_2.The apparent thickness was converted to number of layers using previously elaborated step-height analysis of liquid-exfoliated nanosheets.[15] Raman and photoluminescence spectroscopy was performed on the liquid dispersions using a Horiba Jobin Yvon LabRAM HR800 with 532 nm excitation laser in air under ambient conditions. Great care must be taken during these measurements, as changes in the focal plane during the acquisition will introduce an error in the PL/Raman ratio (see SI Methods). A drop (∼40 μL) of a high concentration dispersion was placed on a glass slide and the drop edge was optically focused using a 10× objective. The focus for the measurement with the 100× objective was readjusted in such a way that the laser was focused slightly above the drop. The average of ∼5 measurements are displayed. Photoluminescence to obtain the contour plot and excitation spectra was measured in quartz cuvettes using an Edinburgh Instruments FS920 PL spectrometer equipped with a Xe lamp (450 W) and a S900 photomultiplier tube detector at room temperature with single monochromators in excitation and emission.

Theoretical Optical Gap Calculations. The optical gap is extracted from the optical conductivity calculated by using the tight-binding propagation method (TBPM).[59,60] We adopt an 11-band TB model of few-layered WS_2 proposed by R. Roldán *et al.* in ref 61, consisting with five d orbitals of W atom and six p orbitals of S atom as the follows:

W atoms: $d_{3z^2-r^2}$, $d_{x^2-y^2}$, d_{xy}, d_{xz}, d_{yz}

S atoms: $p_{x,t}$, $p_{y,t}$, $p_{z,t}$, $p_{x,b}$, $p_{y,b}$, $p_{z,b}$

where the *t* and *b* indexes indicate the top and bottom planes of S atoms within the same layer, respectively. The Slater-Koster parameters used to construct the intralayer W−S, W−W and S−S hopping matrixes are (in unit of eV) $\Delta_0 = -0.872$, $\Delta_1 = 0.42$, $\Delta_2 = -2.065$, $\Delta_p = -3.468$, $\Delta_z = -3.913$, $V_{pd\sigma} = 3.603$, $V_{pd\pi} = -0.942$, $V_{dd\sigma} = -1.216$, $V_{dd\pi} = 0.177$, $V_{dd\delta} = 0.243$, $V_{pp\sigma} = 0.749$, $V_{pp\pi} = 0.236$, and for the interlayer S−S hoppings are $U_{pp\sigma} = -0.55$, $U_{pp\pi} = -0.6$. The spin−orbital couplings originating from the W and S atoms are $\lambda_W = 0.215$, $\lambda_s = 0.057$.

The real part of the optical conductivity at finite frequency is calculated *via* the Kubo's formula as[59−61]

$$\sigma(\omega) = \lim_{\varepsilon\to+0} \frac{1-e^{-\beta\hbar\omega}}{\hbar\omega\Omega} \int_0^\infty dt e^{i(\omega+i\varepsilon)\tau} 2$$
$$i\mathrm{Im}\langle\phi|J[1-f(H)]J(\tau)f(H)|\phi\rangle$$

where Ω is the sample area, $\beta = 1/k_B T$ is the inverse temperature, *H* is the tight-binding Hamiltonian, $f(H) = 1/\{\exp[\beta(H-\mu)]+1\}$ is the Fermi−Dirac distribution operator, and $J(\tau) = \exp(iH\tau/\hbar)J\exp(-iH\tau/\hbar)$ is the current operator in the Heisenberg picture. The state $|\phi\rangle$ is a normalized random state that covers all the eigenstates in the whole spectrum.[59] The time evolution operator and Fermi−Dirac distribution operator are represented as the Chebyshev polynomial expansions.

***Ab Initio* GW-BSE Simulations.** We start the optical calculations using the Kohn−Sham eigenvectors and energy eigenvalues previously calculated within the density-functional theory at generalized-gradient approximation,[62] for monolayer and bilayer WS_2, using plane waves basis set and periodic boundary conditions as implemented in the PWscf[63] and Vasp[64,65] codes. Norm-conserving[66] and PAW[67,68] pseudopotentials are used with a plane wave energy cutoff of 900 eV, with partial-core states included. Atomic coordinates were allowed to relax until all forces were smaller in magnitude than 0.01 eV/Å. Relevant lattice constants (in-plane and out-of-plane) were optimized for each system. To avoid interactions between supercell images, the distance between periodic images of the WS_2 layers along the direction perpendicular to the plane was always larger than 20 Å. Spin−orbit interactions are included in the calculations perturbatively through the calculations of the spinor wave functions, which are used as an input for the calculation of the dielectric functions $\varepsilon_2(\omega,\mathrm{q})$ afterward. The GW-BSE calculations are done using the Yambo code[69] using 300 unoccupied bands in the integration of the self-energy term. The number of *k*-points was chosen according to the Monkhorst−Pack scheme[70] and was set to the equivalent of a 21 × 21 × 1 grid in the primitive unit cell of WS_2, which was previously converged for all structures. The BSE Hamiltonian was created using the ten highest valence bands and the six lowest conduction bands using the Tamm−Dancoff approach. The response functions were obtained in a fine grid of 1000 energy points using a broadening of 0.04 eV in all calculations.

ASSOCIATED CONTENT

Supporting Information

The Supporting Information is available free of charge on the ACS Publications website at DOI: 10.1021/acsnano.5b07228.

Detailed methods, materials characterization and description of a range of cascades. (PDF)

AUTHOR INFORMATION

Corresponding Author

*E-mail: colemaj@tcd.ie.

Notes

The authors declare no competing financial interest.

ACKNOWLEDGMENTS

The research leading to these results has received funding from the European Union Seventh Framework Program under grant agreement no. 604391 Graphene Flagship. We have also

DOI: 10.1021/acsnano.5b07228
ACS Nano XXXX, XXX, XXX−XXX

received support from the Science Foundation Ireland (SFI) funded centre AMBER (SFI/12/RC/2278). In addition, JNC acknowledges the European Research Council (SEMANTICS) and SFI (11/PI/1087) for financial support. CB acknowledges the German research foundation DFG (BA 4856/1-1). VV-M and CG acknowledge Marie Curie ITN network "MoWSeS" (grant no. 317451). EJGS acknowledges the use of computational resources provided by the Extreme Science and Engineering Discovery Environment (XSEDE), supported by NSF grants number TG-DMR120049, TG-DMR150017; as well as the Queen's Fellow Award through the startup grant number M8407MPH. We thank David McAteer for help preparing Figure 1.

REFERENCES

(1) Nicolosi, V.; Chhowalla, M.; Kanatzidis, M. G.; Strano, M. S.; Coleman, J. N. Liquid Exfoliation of Layered Materials. *Science* **2013**, *340*, 1420.

(2) Hernandez, Y.; Nicolosi, V.; Lotya, M.; Blighe, F. M.; Sun, Z.; De, S.; McGovern, I. T.; Holland, B.; Byrne, M.; Gun'Ko, Y. K.; Boland, J. J.; Niraj, P.; Duesberg, G.; Krishnamurthy, S.; Goodhue, R.; Hutchison, J.; Scardaci, V.; Ferrari, A. C.; Coleman, J. N. High-Yield Production of Graphene by Liquid-Phase Exfoliation of Graphite. *Nat. Nanotechnol.* **2008**, *3*, 563−568.

(3) Green, A. A.; Hersam, M. C. Solution Phase Production of Graphene with Controlled Thickness *via* Density Differentiation. *Nano Lett.* **2009**, *9*, 4031−4036.

(4) Coleman, J. N.; Lotya, M.; O'Neill, A.; Bergin, S. D.; King, P. J.; Khan, U.; Young, K.; Gaucher, A.; De, S.; Smith, R. J.; Shvets, I. V.; Arora, S. K.; Stanton, G.; Kim, H.-Y.; Lee, K.; Kim, G. T.; Duesberg, G. S.; Hallam, T.; Boland, J. J.; Wang, J. J.; et al.*et al.* Two-Dimensional Nanosheets Produced by Liquid Exfoliation of Layered Materials. *Science* **2011**, *331*, 568−571.

(5) Zhi, C. Y.; Bando, Y.; Tang, C. C.; Kuwahara, H.; Golberg, D. Large-Scale Fabrication of Boron Nitride Nanosheets and Their Utilization in Polymeric Composites with Improved Thermal and Mechanical Properties. *Adv. Mater.* **2009**, *21*, 2889.

(6) Bourlinos, A. B.; Georgakilas, V.; Zboril, R.; Steriotis, T. A.; Stubos, A. K. Liquid-Phase Exfoliation of Graphite Towards Solubilized Graphenes. *Small* **2009**, *5*, 1841−1845.

(7) Ciesielski, A.; Samori, P. Graphene *via* Sonication Assisted Liquid-Phase Exfoliation. *Chem. Soc. Rev.* **2014**, *43*, 381−398.

(8) Varrla, E.; Backes, C.; Paton, K. R.; Harvey, A.; Gholamvand, Z.; McCauley, J.; Coleman, J. N. Large-Scale Production of Size-Controlled Mos2 Nanosheets by Shear Exfoliation. *Chem. Mater.* **2015**, *27*, 1129−1139.

(9) Paton, K. R.; Varrla, E.; Backes, C.; Smith, R. J.; Khan, U.; O'Neill, A.; Boland, C.; Lotya, M.; Istrate, O. M.; King, P.; Higgins, T.; Barwich, S.; May, P.; Puczkarski, P.; Ahmed, I.; Moebius, M.; Pettersson, H.; Long, E.; Coelho, J.; O'Brien, S. E.; et al.*et al.* Scalable Production of Large Quantities of Defect-Free Few-Layer Graphene by Shear Exfoliation in Liquids. *Nat. Mater.* **2014**, *13*, 624−630.

(10) Hernandez, Y.; Lotya, M.; Rickard, D.; Bergin, S. D.; Coleman, J. N. Measurement of Multicomponent Solubility Parameters for Graphene Facilitates Solvent Discovery. *Langmuir* **2010**, *26*, 3208−3213.

(11) Cunningham, G.; Lotya, M.; Cucinotta, C. S.; Sanvito, S.; Bergin, S. D.; Menzel, R.; Shaffer, M. S. P.; Coleman, J. N. Solvent Exfoliation of Transition Metal Dichalcogenides: Dispersibility of Exfoliated Nanosheets Varies Only Weakly between Compounds. *ACS Nano* **2012**, *6*, 3468−3480.

(12) Lotya, M.; Hernandez, Y.; King, P. J.; Smith, R. J.; Nicolosi, V.; Karlsson, L. S.; Blighe, F. M.; De, S.; Wang, Z. M.; McGovern, I. T.; Duesberg, G. S.; Coleman, J. N. Liquid Phase Production of Graphene by Exfoliation of Graphite in Surfactant/Water Solutions. *J. Am. Chem. Soc.* **2009**, *131*, 3611−3620.

(13) Smith, R. J.; King, P. J.; Lotya, M.; Wirtz, C.; Khan, U.; De, S.; O'Neill, A.; Duesberg, G. S.; Grunlan, J. C.; Moriarty, G.; Chen, J.; Wang, J.; Minett, A. I.; Nicolosi, V.; Coleman, J. N. Large-Scale Exfoliation of Inorganic Layered Compounds in Aqueous Surfactant Solutions. *Adv. Mater.* **2011**, *23*, 3944−3948.

(14) Wu, M.; Wang, Y.; Lin, X.; Yu, N.; Wang, L.; Wang, L.; Hagfeldt, A.; Ma, T. Economical and Effective Sulfide Catalysts for Dye-Sensitized Solar Cells as Counter Electrodes. *Phys. Chem. Chem. Phys.* **2011**, *13*, 19298−301.

(15) Backes, C.; Smith, R. J.; McEvoy, N.; Berner, N. C.; McCloskey, D.; Nerl, H. C.; O'Neill, A.; King, P. J.; Higgins, T.; Hanlon, D.; Scheuschner, N.; Maultzsch, J.; Houben, L.; Duesberg, G. S.; Donegan, J. F.; Nicolosi, V.; Coleman, J. N. Edge and Confinement Effects Allow in Situ Measurement of Size and Thickness of Liquid-Exfoliated Nanosheets. *Nat. Commun.* **2014**, *5*, 4576.

(16) May, P.; Khan, U.; Hughes, J. M.; Coleman, J. N. Role of Solubility Parameters in Understanding the Steric Stabilization of Exfoliated Two-Dimensional Nanosheets by Adsorbed Polymers. *J. Phys. Chem. C* **2012**, *116*, 11393−11400.

(17) Liang, Y. T.; Hersam, M. C. Highly Concentrated Graphene Solutions *via* Polymer Enhanced Solvent Exfoliation and Iterative Solvent Exchange. *J. Am. Chem. Soc.* **2010**, *132*, 17661−17663.

(18) Khan, U.; May, P.; O'Neill, A.; Bell, A. P.; Boussac, E.; Martin, A.; Semple, J.; Coleman, J. N. Polymer Reinforcement Using Liquid-Exfoliated Boron Nitride Nanosheets. *Nanoscale* **2013**, *5*, 581−587.

(19) Bourlinos, A. B.; Georgakilas, V.; Zboril, R.; Steriotis, T. A.; Stubos, A. K.; Trapalis, C. Aqueous-Phase Exfoliation of Graphite in the Presence of Polyvinylpyrrolidone for the Production of Water-Soluble Graphenes. *Solid State Commun.* **2009**, *149*, 2172−2176.

(20) Coleman, J. N. Liquid Exfoliation of Defect-Free Graphene. *Acc. Chem. Res.* **2013**, *46*, 14−22.

(21) Nacken, T. J.; Damm, C.; Walter, J.; Ruger, A.; Peukert, W. Delamination of Graphite in a High Pressure Homogenizer. *RSC Adv.* **2015**, *5*, 57328−57338.

(22) Zhou, K. G.; Mao, N. N.; Wang, H. X.; Peng, Y.; Zhang, H. L. A Mixed-Solvent Strategy for Efficient Exfoliation of Inorganic Graphene Analogues. *Angew. Chem., Int. Ed.* **2011**, *50*, 10839−10842.

(23) Bang, G. S.; Nam, K. W.; Kim, J. Y.; Shin, J.; Choi, J. W.; Choi, S. Y. Effective Liquid-Phase Exfoliation and Sodium Ion Battery Application of Mos2 Nanosheets. *ACS Appl. Mater. Interfaces* **2014**, *6*, 7084−7089.

(24) Alsaif, M.; Balendhran, S.; Field, M. R.; Latham, K.; Wlodarski, W.; Ou, J. Z.; Kalantar-Zadeh, K. Two Dimensional Alpha-Moo3 Nanoflakes Obtained Using Solvent-Assisted Grinding and Sonication Method: Application for H-2 Gas Sensing. *Sens. Actuators, B* **2014**, *192*, 196−204.

(25) Hanlon, D.; Backes, C.; Higgins, T. M.; Hughes, M.; O'Neill, A.; King, P.; McEvoy, N.; Duesberg, G. S.; Mendoza Sanchez, B.; Pettersson, H.; Nicolosi, V.; Coleman, J. N. Production of Molybdenum Trioxide Nanosheets by Liquid Exfoliation and Their Application in High-Performance Supercapacitors. *Chem. Mater.* **2014**, *26*, 1751−1763.

(26) Harvey, A.; Backes, C.; Gholamvand, Z.; Hanlon, D.; McAteer, D.; Nerl, H. C.; McGuire, E.; Seral-Ascaso, A.; Ramasse, Q. M.; McEvoy, N.; Winters, S.; Berner, N. C.; McCloskey, D.; Donegan, J.; Duesberg, G.; Nicolosi, V.; Coleman, J. N. Preparation of Gallium Sulfide Nanosheets by Liquid Exfoliation and Their Application as Hydrogen Evolution Catalysts. *Chem. Mater.* **2015**, *27*, 3483−3493.

(27) Yasaei, P.; Kumar, B.; Foroozan, T.; Wang, C.; Asadi, M.; Tuschel, D.; Indacochea, J. E.; Klie, R. F.; Salehi-Khojin, A. High-Quality Black Phosphorus Atomic Layers by Liquid-Phase Exfoliation. *Adv. Mater.* **2015**, *27*, 1887−1892.

(28) Sresht, V.; Padua, A. A. H.; Blankschtein. Liquid-Phase Exfoliation of Phosphorene: Design Rules from Molecular Dynamics Simulations. *ACS Nano* **2015**, *9*, 8255.

(29) Kang, J.; Wood, J. D.; Wells, S. A.; Lee, J.-H.; Liu, X.; Chen, K.-S.; Hersam, M. C. Solvent Exfoliation of Electronic-Grade, Two-Dimensional Black Phosphorus. *ACS Nano* **2015**, *9*, 3596−3604.

DOI: 10.1021/acsnano.5b07228
ACS Nano XXXX, XXX, XXX−XXX

(30) Brent, J. R.; Savjani, N.; Lewis, E. A.; Haigh, S. J.; Lewis, D. J.; O'Brien, P. Production of Few-Layer Phosphorene by Liquid Exfoliation of Black Phosphorus. *Chem. Commun.* **2014**, *50*, 13338−13341.
(31) Hanlon, D.; Backes, C.; Doherty, E.; Cucinotta, C. S.; Berner, N. C.; Boland, C.; Lee, K.; Lynch, P.; Gholamvand, Z.; Harvey, A.; Zhang, S.; Wang, K.; Moynihan, G.; Pokle, A.; Ramasse, Q. M.; McEvoy, N.; Blau, W. J.; Wang, J.; Abellan, G.; Hauke, F.; et al.*et al.* Liquid Exfoliation of Solvent-Stabilised Few-Layer Black Phosphorus for Applications Beyond Electronics. *Nat. Commun.* **2015**, *6*, 8563.
(32) Naguib, M.; Mashtalir, O.; Carle, J.; Presser, V.; Lu, J.; Hultman, L.; Gogotsi, Y.; Barsoum, M. W. Two-Dimensional Transition Metal Carbides. *ACS Nano* **2012**, *6*, 1322−1331.
(33) Zhou, K.; Jiang, S.; Bao, C.; Song, L.; Wang, B.; Tang, G.; Hu, Y.; Gui, Z. Preparation of Poly(Vinyl Alcohol) Nanocomposites with Molybdenum Disulfide (Mos2): Structural Characteristics and Markedly Enhanced Properties. *RSC Adv.* **2012**, *2*, 11695−11703.
(34) Paton, K. R.; Varrla, E.; Backes, C.; Smith, R. J.; Khan, U.; O'Neill, A.; Boland, C.; Lotya, M.; Istrate, O. M.; King, P.; Higgins, T.; Barwich, S.; May, P.; Puczkarski, P.; Ahmed, I.; Moebius, M.; Pettersson, H.; Long, E.; Coelho, J.; O'Brien, S. E.; et al.*et al.* Scalable Production of Large Quantities of Defect-Free Few-Layer Graphene by Shear Exfoliation in Liquids. *Nat. Mater.* **2014**, *13*, 624−30.
(35) Eksik, O.; Gao, J.; Shojaee, S. A.; Thomas, A.; Chow, P.; Bartolucci, S. F.; Lucca, D. A.; Koratkar, N. Epoxy Nanocomposites with Two-Dimensional Transition Metal Dichalcogenide Additives. *ACS Nano* **2014**, *8*, 5282−5289.
(36) Sorrentino, A.; Altavilla, C.; Merola, M.; Senatore, A.; Ciambelli, P.; Iannace, S. Nanosheets of Mos2-Oleylamine as Hybrid Filler for Self-Lubricating Polymer Composites: Thermal, Tribological, and Mechanical Properties. *Polym. Compos.* **2015**, *36*, 1124−1134.
(37) May, P.; Khan, U.; O'Neill, A.; Coleman, J. N. Approaching the Theoretical Limit for Reinforcing Polymers with Graphene. *J. Mater. Chem.* **2012**, *22*, 1278−1282.
(38) Wang, J.-Z.; Lu, L.; Lotya, M.; Coleman, J. N.; Chou, S.-L.; Liu, H.-K.; Minett, A. I.; Chen, J. Development of Mos2-Cnt Composite Thin Film from Layered Mos2 for Lithium Batteries. *Adv. Energy Mater.* **2013**, *3*, 798−805.
(39) Pumera, M.; Sofer, Z.; Ambrosi, A. Layered Transition Metal Dichalcogenides for Electrochemical Energy Generation and Storage. *J. Mater. Chem. A* **2014**, *2*, 8981−8987.
(40) Woodward, R. I.; Kelleher, E. J. R.; Howe, R. C. T.; Hu, G.; Torrisi, F.; Hasan, T.; Popov, S. V.; Taylor, J. R. Tunable Q-Switched Fiber Laser Based on Saturable Edge-State Absorption in Few-Layer Molybdenum Disulfide (Mos2). *Opt. Express* **2014**, *22*, 31113−31122.
(41) Zhang, M.; Howe, R. T.; Woodward, R.; Kelleher, E. R.; Torrisi, F.; Hu, G.; Popov, S.; Taylor, J. R.; Hasan, T. Solution Processed Mos2-Pva Composite for Sub-Bandgap Mode-Locking of a Wideband Tunable Ultrafast Er:Fiber Laser. *Nano Res.* **2015**, *8*, 1522−1534.
(42) Sun, Z.; Hasan, T.; Torrisi, F.; Popa, D.; Privitera, G.; Wang, F.; Bonaccorso, F.; Basko, D. M.; Ferrari, A. C. Graphene Mode-Locked Ultrafast Laser. *ACS Nano* **2010**, *4*, 803−810.
(43) Khan, U.; O'Neill, A.; Porwal, H.; May, P.; Nawaz, K.; Coleman, J. N. Size Selection of Dispersed, Exfoliated Graphene Flakes by Controlled Centrifugation. *Carbon* **2012**, *50*, 470−475.
(44) Jaramillo, T. F.; Jorgensen, K. P.; Bonde, J.; Nielsen, J. H.; Horch, S.; Chorkendorff, I. Identification of Active Edge Sites for Electrochemical H-2 Evolution from Mos2 Nanocatalysts. *Science* **2007**, *317*, 100−102.
(45) Torrisi, F.; Coleman, J. N. Electrifying Inks with 2d Materials. *Nat. Nanotechnol.* **2014**, *9*, 738−739.
(46) Kang, J.; Seo, J.-W. T.; Alducin, D.; Ponce, A.; Yacaman, M. J.; Hersam, M. C. Thickness Sorting of Two-Dimensional Transition Metal Dichalcogenides *via* Copolymer-Assisted Density Gradient Ultracentrifugation. *Nat. Commun.* **2014**, *5*, 5478.
(47) O'Neill, A.; Khan, U.; Coleman, J. N. Preparation of High Concentration Dispersions of Exfoliated Mos2 with Increased Flake Size. *Chem. Mater.* **2012**, *24*, 2414−2421.
(48) Barwich, S.; Khan, U.; Coleman, J. N. A Technique to Pretreat Graphite Which Allows the Rapid Dispersion of Defect-Free Graphene in Solvents at High Concentration. *J. Phys. Chem. C* **2013**, *117*, 19212−19218.
(49) Kouroupis-Agalou, K.; Liscio, A.; Treossi, E.; Ortolani, L.; Morandi, V.; Pugno, N. M.; Palermo, V. Fragmentation and Exfoliation of 2-Dimensional Materials: A Statistical Approach. *Nanoscale* **2014**, *6*, 5926−5933.
(50) Lin, Y.; Ling, X.; Yu, L.; Huang, S.; Hsu, A. L.; Lee, Y.-H.; Kong, J.; Dresselhaus, M. S.; Palacios, T. Dielectric Screening of Excitons and Trions in Single-Layer Mos2. *Nano Lett.* **2014**, *14*, 5569−5576.
(51) Zhao, W.; Ghorannevis, Z.; Chu, L.; Toh, M.; Kloc, C.; Tan, P.-H.; Eda, G. Evolution of Electronic Structure in Atomically Thin Sheets of Ws2 and Wse2. *ACS Nano* **2012**, *7*, 791−797.
(52) Zhu, B.; Chen, X.; Cui, X. Exciton Binding Energy of Monolayer Ws2. *Sci. Rep.* **2015**, *5*, 9218.
(53) Scheuschner, N.; Ochedowski, O.; Kaulitz, A.-M.; Gillen, R.; Schleberger, M.; Maultzsch, J. Photoluminescence of Freestanding Single- and Few-Layer Mos2. *Phys. Rev. B: Condens. Matter Mater. Phys.* **2014**, *89*, 125406.
(54) Mak, K. F.; Lee, C.; Hone, J.; Shan, J.; Heinz, T. F. Atomically Thin Mos2. A New Direct-Gap Semiconductor. *Phys. Rev. Lett.* **2010**, *105*, 136805.
(55) Splendiani, A.; Sun, L.; Zhang, Y.; Li, T.; Kim, J.; Chim, C.-Y.; Galli, G.; Wang, F. Emerging Photoluminescence in Monolayer Mos2. *Nano Lett.* **2010**, *10*, 1271−1275.
(56) Gutiérrez, H. R.; Perea-López, N.; Elías, A. L.; Berkdemir, A.; Wang, B.; Lv, R.; López-Urías, F.; Crespi, V. H.; Terrones, H.; Terrones, M. Extraordinary Room-Temperature Photoluminescence in Triangular Ws2Monolayers. *Nano Lett.* **2012**, *13*, 3447−3454.
(57) Kobayashi, Y.; Sasaki, S.; Mori, S.; Hibino, H.; Liu, Z.; Watanabe, K.; Taniguchi, T.; Suenaga, K.; Maniwa, Y.; Miyata, Y. Growth and Optical Properties of High-Quality Monolayer Ws2 on Graphite. *ACS Nano* **2015**, *9*, 4056−4063.
(58) Saakov, V. S.; Drapkin, V. Z.; Krivchenko, A. I.; Rozengart, E. V.; Bogachev, Y. V.; Knyazev, M. N. *Derivative Spectrophotometry and Electron Spin Resonance (ESR) Spectroscopy for Ecological and Biological Questions*; Springer-Verlag: Weinheim, 2013.
(59) Yuan, S.; De Raedt, H.; Katsnelson, M. I. Modeling Electronic Structure and Transport Properties of Graphene with Resonant Scattering Centers. *Phys. Rev. B: Condens. Matter Mater. Phys.* **2010**, *82*, 115448.
(60) Yuan, S.; Roldán, R.; De Raedt, H.; Katsnelson, M. I. Optical Conductivity of Disordered Graphene Beyond the Dirac Cone Approximation. *Phys. Rev. B: Condens. Matter Mater. Phys.* **2011**, *84*, 195418.
(61) Roldán, R.; López-Sancho, M. P.; Guinea, F.; Cappelluti, E.; Silva-Guillén, J. A.; Ordejón, P. Momentum Dependence of Spin−Orbit Interaction Effects in Single-Layer and Multi-Layer Transition Metal Dichalcogenides. *2D Mater.* **2014**, *1*, 034003.
(62) Perdew, J. P.; Burke, K.; Ernzerhof, M. Generalized Gradient Approximation Made Simple. *Phys. Rev. Lett.* **1996**, *77*, 3865−3868.
(63) Giannozzi, P.; Baroni, S.; Bonini, N.; Calandra, M.; Car, R.; Cavazzoni, C.; Ceresoli, D.; Chiarotti, G. L.; Cococcioni, M.; Dabo, I.; Dal Corso, A.; de Gironcoli, S.; Fabris, S.; Fratesi, G.; Gebauer, R.; Gerstmann, U.; Gougoussis, C.; Kokalj, A.; Lazzeri, M.; Martin-Samos, L.; et al.*et al.* Quantum Espresso: A Modular and Open-Source Software Project for Quantum Simulations of Materials. *J. Phys.: Condens. Matter* **2009**, *21*, 395502.
(64) Kresse, G.; Furthmuller, J. Efficient Iterative Schemes for Ab Initio Total-Energy Calculations Using a Plane-Wave Basis Set. *Phys. Rev. B: Condens. Matter Mater. Phys.* **1996**, *54*, 11169−11186.
(65) Kresse, G.; Hafner, J. Ab-Initio Molecular-Dynamics for Open-Shell Transition-Metals. *Phys. Rev. B: Condens. Matter Mater. Phys.* **1993**, *48*, 13115−13118.
(66) Troullier, N.; Martins, J. L. Efficient Pseudopotentials for Plane-Wave Calculations. *Phys. Rev. B: Condens. Matter Mater. Phys.* **1991**, *43*, 1993−2006.

DOI: 10.1021/acsnano.5b07228
ACS Nano XXXX, XXX, XXX−XXX

(67) Blochl, P. E. Projector Augmented-Wave Method. *Phys. Rev. B: Condens. Matter Mater. Phys.* **1994**, *50*, 17953−17979.
(68) Kresse, G.; Joubert, D. From Ultrasoft Pseudopotentials to the Projector Augmented-Wave Method. *Phys. Rev. B: Condens. Matter Mater. Phys.* **1999**, *59*, 1758−1775.
(69) Marini, A.; Hogan, C.; Gruening, M.; Varsano, D. Yambo: An Ab Initio Tool for Excited State Calculations. *Comput. Phys. Commun.* **2009**, *180*, 1392−1403.
(70) Monkhorst, H. J.; Pack, J. D. Special Points for Brillouin-Zone Integrations. *Phys. Rev. B* **1976**, *13*, 5188−5192.

DOI: 10.1021/acsnano.5b07228
ACS Nano XXXX, XXX, XXX−XXX